Sea Ice Detection Using U.K. TDS-1 GNSS-R Data

Alberto Alonso-Arroyo, *Student Member, IEEE*, Valery U. Zavorotny, *Fellow, IEEE*, and Adriano Camps, *Fellow, IEEE*

***Abstract*— A sea ice detection algorithm developed using the U.K. TechDemoSat-1 (U.K. TDS-1) global navigation satellite systems (GNSSs)-reflectometry data over the Arctic and Antarctic regions is presented. It is based on measuring the similarity of the received GNSS reflected waveform or delay Doppler map (DDM) to the coherent reflection model waveform. Over the open ocean, the scattered signal has a diffusive, incoherent nature; it is described by the rough surface scattering model based on the geometric optics and the Gaussian statistics for the ocean surface slopes. Over sea ice and, in particular, newly formed sea ice, the scattered signal acquires a coherence, which is characteristic for a surface with large flat areas. In order to measure the similarity of the received waveform or DDM, to the coherent reflection model, three different estimators are presented: the normalized DDM average, the trailing edge slope (TES), and the matched filter approach. Here, a probabilistic study is presented based on a Bayesian approach using two different and independent ground-truth data sets. This approach allows one to thoroughly assess the performance of the estimators. The best results are achieved for both the TES and the matched filter approach with a probability of detection of 98.5%, a probability of false alarm of $\sim$ 3.6%, and a probability of error of 2.5%. However, the matched filter approach is preferred due to its simplicity. Data from AMSR2 processed using the Arctic Radiation and Turbulence Interaction STudy Sea Ice algorithm and from an Special Sensor Microwave Imager/Sounder radiometer processed by Ocean and Sea Ice SAF have been used as ground truth. A pixel has been classified as a sea ice pixel if the sea ice concentration (SIC) in it was larger than 15%. The measurement of the SIC is also assessed in this paper, but the nature of the U.K. TDS-1 data (lack of calibrated data) does not allow to make any specific conclusions about the SIC.**

***Index Terms*— Coherent scattering, global navigation satellite systems-reflectometry (GNSS-R), incoherent scattering, sea ice, U.K. TechDemoSat-1 (U.K. TDS-1).**

I. Introduction

ACTIVE and passive remote sensing techniques have been used to monitor sea ice. Passive techniques based on microwave radiometry have been used to determine the sea ice concentration (SIC) parameter, which is the percentage of ice on a pixel [1]. For instance, 0% indicates open water, 50% indicates that half of the pixel is covered by ice, and 100% indicates that the entire pixel is solid ice [2]. Active techniques based on real or synthetic aperture radars (SARs) generally measure surface roughness, which leads to sea ice type classification, as the waveform shape is highly sensitive to surface roughness [3]. However, in order to achieve high altimetric resolution, the frequency bands used are normally Ku-band or K-band (12–18 and 18–26 GHz, respectively), which make the radar technique sensitive to small-($\sim$ cm) and large-($\sim$ m) scale roughness [4].

The idea of using the global navigation satellite system (GNSS) signals of opportunity for remote sensing purposes was first discussed in the late 1980s [5]. One of its direct applications is the use of GNSS reflected signals for mesoscale altimetry, as proposed in 1993 with the passive reflectometry and interferometry system concept [6]–[8]. It is a passive technique, because it uses the GNSS signals already transmitted by the GNSS satellites for navigation purposes and only a receiver is needed. In 2000, initial results comparing the waveform peak power of the GNSS reflected signals over ice against RADARSAT backscattering echoes were presented [9]. In 2003, a theoretical model explaining the ice scattering mechanism was proposed [10]. In 2006, it was shown that there is a strong presence of the coherent component in the GNSS-reflectometry (GNSS-R) sea ice bistatic scattering echoes [11], indicating a deficiency of a purely diffusive scattering model. This was confirmed in 2010 with a detailed study using the United Kingdom Disaster Monitoring Constellation (U.K.-DMC) GNSS-R data set [12]. However, unambiguous relations between waveform peak power or shape and sea ice parameters have not been found. Airborne studies using GNSS-R data were also performed in 2010 for the determination of sea ice parameters [13]. Also, the effect of surface roughness was analyzed and compared with lidar measurements in [13].

In this paper, the use of GNSS reflected signals for sea ice detection with simple and straightforward algorithms that can be implemented on future spaceborne platforms is proposed and demonstrated. Section II shows the theoretical background that justifies the analysis performed in this paper. Section III describes the approach followed, which is based on the experimental data obtained from the U.K. TechDemoSat-1 (U.K. TDS-1) mission. Section IV describes the ground-truth data used to validate the analysis performed. Section V evaluates the GNSS-R approach with the available ground-truth data. Section VI discusses the results achieved, the error sources, and the applicability of the proposed techniques. Finally, Section VII presents the conclusions of this paper.

Manuscript received March 2, 2016; revised May 26, 2016, October 26, 2016, and February 16, 2017; accepted April 21, 2017. Date of publication June 13, 2017; date of current version August 25, 2017. This work was supported by the Spanish Ministry of Economy and Competitiveness under Project AYA2011-29183-C02-01 (Advanced Radio Ocultations and Scatterometry Applications using GNSS and other opportunity signals) and Project ESP2015-70014-C2-1-R. The work of A. Alonso-Arroyo was supported by the Fulbright Commission in Spain through a Fulbright Grant. *(Corresponding author: Alberto Alonso-Arroyo.)*

A. Alonso-Arroyo is with the Department of Signal Theory and Communications, Universitat Politècnica de Catalunya, BarcelonaTech, and also with the NOAA Earth System Research Laboratory, Physical Science Division, Boulder, CO 80305 USA (e-mail: alberto.alonso.arroyo@tsc.upc.edu).

V. U. Zavorotny is with the NOAA Earth System Research Laboratory, Physical Science Division, Boulder, CO 80305 USA (e-mail: valery.zavorotny@noaa.gov).

A. Camps is with the Department of Signal Theory and Communications, Universitat Politècnica de Catalunya-BarcelonaTech, 08034 Barcelona, Spain (e-mail: camps@tsc.upc.edu).

Color versions of one or more of the figures in this paper are available online at http://ieeexplore.ieee.org.

Digital Object Identifier 10.1109/TGRS.2017.2699122

II. Theoretical Background

Conventional satellite radar altimetry has been used for sea ice studies since the early 1980's [14], [15]. It relies on the scattering of EM waves from the surface while the radar antenna is looking at nadir. In that situation, the power waveform or returned power as a function of the delay is composed of three distinct components [14], [16], [17]

$$W(t) = S_r(t) * P_{\mathrm{FS}}(t) * r(t) \tag{1}$$

where $S_r(t)$ is the shape of the transmitted pulse or point target response, $P_{\mathrm{FS}}(t)$ is the flat surface response, which is the radar cross section as a function of the delay time (over the horizontal surface) weighted by the gain pattern, and $r(t)$ characterizes the surface roughness, and it is the mean density of point scatterers as a function of the delay time. In other words, $S_r(t)$ is a Doppler cut of the so-called Woodward ambiguity function (WAF) [18] through its maximum. $P_{\mathrm{FS}}(t)$ depends on the antenna pattern and the radar cross section, which at the same time depends on the probability density function (pdf) of the surface's slopes at L-band [19]. It determines the trailing edge shape of the waveform while it affects also the leading edge shape. Finally, $r(t)$ characterizes the surface roughness parameter, and it is the main contributor to the leading edge shape although it does not affect so severely the trailing edge.

In the particular case of conventional GNSS-R (cGNSS-R) for the public C/A-code signal, the equivalent radar pulsewidth is approximately 300 m (1 chip). This means that, unless there is a significant variation of surface topography (or in the distribution or point scatterers), (1) can be approximated by

$$W(t) = S_r(t) * P_{\mathrm{FS}}(t) \tag{2}$$

since the radar pulsewidth is much larger than the immediate *rms* elevations. Note that a nadir-looking geometry is a particular case of the forward-scattering mechanism found in GNSS-R, and consequently, part of the previous work performed for satellite radar altimetry can be used. Therefore, the waveform model shown in (2) is a particular case of the waveform/delay Doppler map (DDM) model proposed by Zavorotny and Voronovich [19] to determine the shape of the rough ocean scattered signals

$$W(\tau, f_D) = \int \frac{D^2(\vec{\rho})\Lambda^2(\tau - (R_r(\vec{\rho}) + R_t(\vec{\rho}))/c)q^4(\vec{\rho})}{4{R_r}^2(\vec{\rho}){R_t}^2(\vec{\rho})q_z^4(\vec{\rho})} \times |\Gamma(\vec{\rho})|^2 {T_c}^2 |S(f_D(\vec{\rho}) - f_c)|^2 P\left(-\frac{q_\perp(\vec{\rho})}{q_z(\vec{\rho})}\right) d^2\rho \tag{3}$$

where T_c stands for the coherent integration time, Γ for the Fresnel reflection coefficient, the WAF is approximated by a triangular function Λ in the time domain and by a *sinc* function S in the frequency domain, q stands for the scattering vector, ρ is a vector from the specular reflection point to the scattering point, R_r is the distance between the scattering point and the receiver, R_t is the distance between the transmitter and the scattering point, q_z is the vertical component of the scattering vector, $q_\perp$ is the absolute value of the x and y components of the scattering vector, and $P(\vec{v})$ is the pdf of the surface slopes. Note that this model is based on the Kirchoff-approximation geometric optics, like (1), and only takes into account the noncoherent component, assuming that the coherent component is negligible. Equation (3) can be expressed in a simplified form as in [20]–[22]

$$W(\tau, f_D) \triangleq |\chi(\tau, f_D)|^2 ** |\sigma^0(\tau, f_D)|^2 \tag{4}$$

where f_D takes into account the power spreading in the Doppler domain, χ stands for the WAF, σ^0 for the normalized bistatic radar cross section which already includes the antenna pattern projection over the surface, the distance parameters, and the surface parameters, such as the pdf of the surface slopes, and $**$ expresses a 2-D convolution in both domains, τ and f_D. A cut of (4) over the Doppler domain results in the so-called waveform, and makes (2) and (4) equivalent. In both altimetric and GNSS-R models, only surface scattering is taken into account since volume scattering compared to surface scattering from relatively thin first-year sea ice at L-band can be neglected [23], [24].

Although different theoretical models were proposed, no experimental cGNSS-R waveforms obtained from space were available until 2005 with the launch of the U.K.-DMC satellite [11]. Therein, it is observed that the waveforms reflected from the ocean surface and from the sea ice were significantly different. While over the ocean, there was a noticeable delay-Doppler spreading of the signal power scattered, which led to the "horseshoe" shape, the DDM from a signal scattered off sea ice resembled the WAF itself, without any delay-Doppler spreading. For several regions, the phase of the reflected signal at the DDM peak could be tracked, even identifying the navigation bits, which indicates the presence of a strong coherent component [11]. This demonstrated experimentally that the assumption of a negligible coherent component is mostly valid for the sea surface, but not for the sea ice surface. In [15, Fig. 2], this fact was conceptually illustrated for near-normal incidence angle, computing the near-normal incidence scattering cross section for both the coherent and incoherent components. Therein, it is seen that the pdf of the slopes is much narrower for the sea ice than for the open sea, tending to a delta function centered at zero for new ice. In other words, for all practical purposes, the surface is flat and only coherent scattering occurs. The DDM model for the coherent component was introduced in [25]. Instead of a convolution, as shown in (4), it is a product between the WAF and the surface reflectivity, times the factor that takes into account the loss of the spatial coherence due to the presence of some relatively weak surface roughness [4], [26]. The general mathematical expression for the coherent scattered waveform is

$$W(\tau, f_D) \propto {T_c}^2 |\Gamma(\vec{\rho})|^2 e^{-4k^2\sigma_h^2 \cos^2(\theta_{\mathrm{inc}})} |S(f_D(\vec{\rho}) - f_c)|^2 \times \frac{D^2(\vec{\rho})\Lambda^2(\tau - (R_r(\vec{\rho}) + R_t(\vec{\rho}))/c)}{(4\pi(R_r(\vec{\rho}) + R_t(\vec{\rho})))^2}. \tag{5}$$

A deeper analysis of the sea ice signals scattered using the U.K.-DMC data was presented in [12], where again the waveforms' shape indicated the presence of a coherent component. No clear relations between waveform observables and sea ice parameters were demonstrated. Unfortunately, the

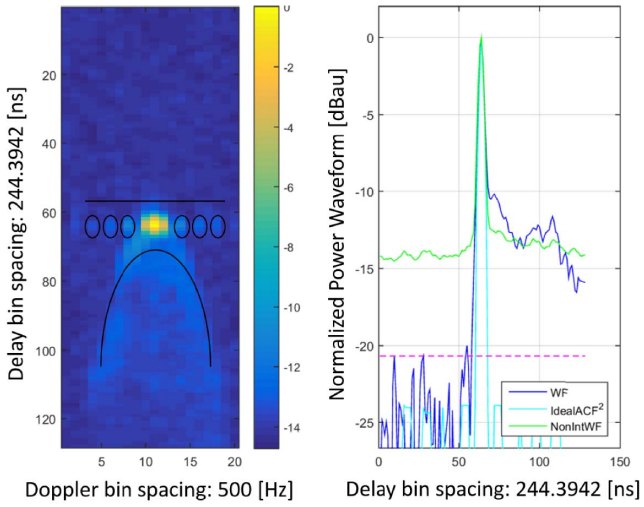

(a)

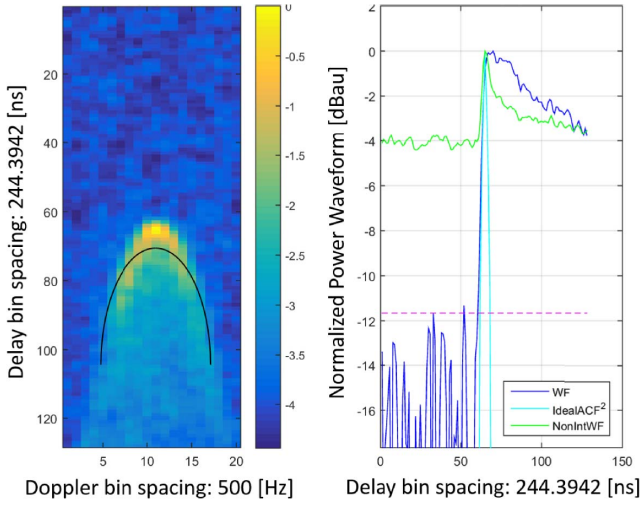

(b)

Fig. 1. Two DDMs and the corresponding waveforms for (a) sea ice and (b) open water regions. (Left) Colorbar is expressed in decibel units. (Right) WF stands for the DIW, IdealICF^2 for the code autocorrelation function squared, and NonIntWF for a Doppler cut of the DDM through its maximum.

nature of the U.K. TDS-1 data (lack of calibrated data) does not allow us to make any specific conclusions about the SIC. Nevertheless, this paper provides a preliminary demonstration of the potential of GNSS reflectometry over sea ice.

III. GNSS-R Approach

A. "K-Shape" DDM Concept

After analyzing several data sets from the U.K. TDS-1, it was detected that the shape of the measured DDM was different depending on the characteristics of the surface the GNSS signal was scattered off. Fig. 1 shows two different extracts of the data retrieved from February 19, 2015 using the receiver specifications identification number RD000019 and the tracklist identification number TD000071. Fig. 1(a) and (b) corresponds to data from the Northern Hemisphere (Arctic), and their spatial distance is less than 60 km, as there is only 10 s difference among their acquisition. In Fig. 1(a) (left), it is possible to see the DDM from a signal scattered off a sea ice-covered surface. Particularly, the distribution of the power in the DDM resembles the shape of the letter "K" (rotated 90°). Therein, it is possible to identify two different features. One of them is the vertical element of the "K" (horizontal line on the image), stretching along the Doppler frequency axis and depicting a partially coherent DDM component. It corresponds to the WAF multiplied by the reflectivity, times second-order coherence function ($e^{-4k^2\sigma_h^2\cos^2(\theta_{inc})}$) [26]. The rest of the DDM, which spans over the delay-Doppler domain with the "horseshoe" shape, corresponds to the incoherent component. For that particular DDM, that region has power levels similar to the WAF Doppler sidelobes, which are at least 13 dB below its maximum, indicating that the coherent component was the main scattering mechanism. In Fig. 1(a) (right), the Doppler integrated waveform (DIW) in blue, a Doppler cut of the WAF in cyan, which is called IdealACF^2, and a Doppler cut of the DDM in green are shown. The DIW is the integral of the DDM over the Doppler domain. This is a way to see the power spreading due to surface roughness, but only in one dimension (the delay domain). Without doing that, the spreading of the power over the delay domain is barely noticeable, as it can be seen on the Doppler cut shown in the same figure in green. The leading edge is not affected by surface roughness due to the large pulsewidth of the GNSS signals and the low roughness conditions. Also, due to the integral over the Doppler domain, the incoherent scattered power is better observed, because the DIW takes into account the power scattered at the same delay for all Doppler shifts, and the thermal noise variability is reduced. This could be barely seen on the conventional waveform (green), since only one Doppler bin is considered.[1] It comes from a residual incoherent mechanism, because in a purely coherent scattering mechanism, the waveform power level after the peak value should go down again to the thermal noise mean level. However, it is one order of magnitude smaller than the coherent one, and therefore, the coherent scattering mechanism is the dominating one. On the contrary, Fig. 1(b) shows a totally different effect. Therein, only the "horseshoe" shape of the DDM is seen and the WAF Doppler sidelobes are no longer present. Also, even though the "horseshoe" shape of the DDM is an indicator of the surface roughness, the shape of the waveform's leading edge is barely affected, which occurs due to the small bandwidth of the C/A code. Conversely, the trailing edge of the DIW is very different. In Fig. 1(a), there are two different regions on the trailing edge, one where the slope is very large and follows the WAF shape (associated to the coherent component), and one where the slope is smoother and corresponds to the incoherent

[1]The Doppler domain integration of the DDM is needed only occasionally for GNSS-R spaceborne data, as due to the geometry and the platform's relatively high speed, the power is largely spread on the Doppler domain. Note that the Global Positioning System (GPS) satellite effective speed is much smaller than the platform's effective speed. For the airborne case, since the platform's speed is much lower, the Doppler spreading is not as large as the spaceborne case, and the waveform shows all the sensitivity to surface roughness on the trailing edge slope (TES) [19], without the need of a Doppler integral. Note that the slope of the DIW was proposed as an indicator of the ocean's *mss* [19].

power. In Fig. 1(b), there is only one smooth region that can be identified, which indicates the lack of coherent power, since there is no large power drop after the WAF peak value.

These features are seen in most of the data gathered from the U.K. TDS-1, and indicate that two different scattering mechanisms affect the scattering off sea ice or open water. When the reflection is purely coherent, there is no delay-Doppler spreading, and the reflected waveform is the WAF multiplied by the power Fresnel reflection coefficient. If the reflection is purely incoherent, there is a large delay-Doppler spreading. The spreading depends on the roughness and, in particular, on the pdf of the slopes at the L-band. It might be logical that when the reflection has a coherent part and a noncoherent part, the waveform can be approximated by a linear combination of both models, as shown in Fig. 1(a) and also identified in [27]. The more coherent the reflection is, the more it will tend to the WAF shape. The more incoherent the reflection is, the more it will tend to the model in [19]. The combination of both models tends to the "K-shape" DDM model. The larger the coherent component, the smaller the incoherent one, and vice versa [4].

It has been shown both theoretically [19] and empirically [11], [28]–[30] that under open ocean conditions, even at weak winds, the surface can be nearly always considered rough, and the coherent component negligible [19]. On the other hand, there is no correct theoretical model that matches the waveforms obtained from the sea ice. The coherent component can be introduced into the noncoherent model in two different ways. The first one could be comprised of a bistatic radar equation (3) as a DDM incoherent part plus a separate DDM term, which describes a coherent (or partially coherent) component. The second one is to devise a single bistatic radar equation, which would have, under the surface integral, a single combined bistatic radar cross section similar to that in [31]. The equivalent bistatic cross section will consist of a sum of two terms: one, the same as in (3) describing the incoherent diffuse scattering, and another, describing the coherent reflection from the flat component of the surface. Formally, this can be done, and previously, this approach was used for simulating the coherent and incoherent received scattered power under the bistatic geometry for soil moisture monitoring purposes [31], [32]. However, it makes the combined bistatic radar cross section distance and antenna parameters-dependent [32], [33].

B. Definition of the GNSS-R Observables

There are several approaches that have been used previously to match simulated GNSS-R data with real data in order to retrieve the geophysical parameters. One of the most common ones is the waveform fitting [28], [34], [35], which consists of minimizing the cost function created using measured data and simulated data. This one has been widely used for the retrieval of wind-speed data over the ocean. Other heuristic approaches have been used in order to infer the surface roughness, such as the volume under the normalized DDM (V_{DDM}), or the area under the normalized waveform (A_{WF}) [36]. Also, different heuristic approaches have been compared against the wind speed over the ocean, such as the DDM average (DDMA), the DDM variance (DDMV), the Allan DDMV (ADDMV), the leading edge slope (LES), and the TES [37]. In [36], it was already stated that the correlation between the (V_{DDM}), which can be seen as the DDMA for a large delay-Doppler region, and the TES was 0.74.

The U.K. TDS-1 data are DDMs time referenced and geolocated with a coherent integration time of 1 ms and an incoherent integration time of 1 s. In other words, there is no access to the 1-ms complex DDMs generated in the operation to obtain the 1 s incoherently integrated DDM, and therefore, there is no phase information. The delay bin is approximately 244 ns, and the Doppler bin is 500 Hz. Consequently, any operation that can be done among 1 ms coherently integrated complex DDMs, such as the DDMV or the ADDMV, must be discarded. Data from the U.K. TDS-1 are not calibrated, since there is no information about the direct signal power impinging on the ground or about the direct signal power at the satellite level. This prevents the use of parameters, such as the signal-to-noise ratio (SNR), as the transmitted power depends on the satellite used and may vary with time. Consequently, all DDMs retrieved from the U.K. TDS-1 have been normalized to their maxima. So, the CYclone GNSS (CYGNSS) approach to the wind-speed retrieval based on the signal power received cannot be applied to the U.K. TDS-1 data [38], [39].

The lack of a simple theoretical model for sea ice surface forward scattering at the L-band that determines both the coherent and incoherent scattered power prevents us from applying the cost function approach. However, initially, we will measure the similarity to the coherent waveform in order to determine the sea ice presence, so a comparison with the full coherent scattering model will be performed. The following three heuristic approaches will be used, which basically measure the peakedness of the WAF or its similarity to the coherent model.

1) *DDMA:* It is the average value of the normalized DDM around its peak. For this analysis, three different regions on the DDM have been selected.
   a) 3×3*:* 3 Doppler bin cells $\times$ 3 delay bin cells.
   b) 3×5*:* 3 Doppler bin cells $\times$ 5 delay bin cells.
   c) 3×7*:* 3 Doppler bin cells $\times$ 7 delay bin cells.
2) *TES:* It is the slope computed between the maximum of the normalized DIW and its value at different delay bins. For this analysis, three different versions have been selected.
   a) *Three-Bin:* Approximately 750 ns after the peak power.
   b) *Six-Bin:* Approximately 1.5 μs after the peak power.
   c) *Nine-Bin:* Approximately 2.25 μs after the peak power.
3) *MF:* Also known as correlation approach, it computes how similar the unitary energy DIW waveform is to the unitary energy WAF Doppler cut for the same pseudorandom noise code or coherent scattering model.

The results obtained with the LES estimator were less satisfactory than others and, therefore, are not presented in this paper.

Similar observables for sea ice detection and classification have been used in conventional altimetry, such as the SIGPK, which is the peak backscatter power in the returned echo, and the SIGTD, which is the average power computed between eight early and eight late delay bins of the DIW [40]. Note that the SIGTD is similar to the DDMA approach, and it is a measurement of the signal/waveform peakedness, or how coherent is the echo returned. Also note that the SIGPK cannot be used with the U.K. TDS-1 data due to the lack of calibrated data. Other authors have also developed different algorithms for the waveform shape detection, such as the pulse peakiness [41]–[43], which are similar to the DDMA algorithm and basically measure how different the waveform is from the incoherent model.

IV. Ground-Truth Description

In order to detect the presence of sea ice and compare it to the GNSS-R waveform shape, two different ground-truth SIC data sets have been used. The first one is the Arctic Radiation and Turbulence Interaction STudy Sea Ice (ASI) algorithm [1] using AMSR2 data. The second one is the Ocean and Sea Ice SAF (OSISAF) [2], which is computed using data from the different channels of the Special Sensor Microwave Imager/Sounder (SSMIS) sensor.

A. ASI Algorithm Using AMSR2 Data

The ASI algorithm was originally developed to use the high resolution product provided by the 85-GHz channel of the SSM/I sensor. Herein, it is applied to the AMSR2 data, which was launched on May 18, 2012. The AMSR2 is a multifrequency microwave radiometer with channels at 6.93, 7.3, 10.65, 18.7 23.8, 36.5, and 89 GHz. The SIC is calculated from the polarization difference of the 89-GHz channel. The ASI algorithm is based on the polarization difference of the H and V channels ($P = T_{\mathrm{BV}} - T_{\mathrm{BH}}$). At 89 GHz, the polarization difference for all types of ice is very small, either first-year, multiyear, or pure ice, whereas for open water it is much larger. The SIC is determined by a linear model, which decomposes the polarization difference in the contribution from open water and the contribution of sea ice. Both of them are multiplied by a term that depends on the SIC. The lower the polarization difference, the larger the SIC and vice versa. Using this model, a third degree polynomial is finally fitted to obtain the SIC as a function of the polarization difference. However, the 89-GHz frequency band is highly prone to atmospheric effects. Even though they have a poorer resolution, the lower frequency channels of the AMSR2 data are used to assess the quality of the retrievals obtained from the 89-GHz channel, taking into account atmospheric effects and discarding data without sufficient quality. The SIC maps[2] used as a ground truth for the analysis developed along this paper are obtained from [44]. For more information about the ASI algorithm, see [1].

[2]Those maps are given in the polar stereographic coordinates for both hemispheres (Northern and Southern) using a grid resolution of 6.25 km. This implies that the GNSS-R data are converted into those coordinates in order to make the appropriate comparisons.

B. OSI SAF Data

The OSISAF algorithm is based on the combination of the data provided by the different channels of the SSMIS radiometer, in particular the 19, 37, and 91 GHz. The combination is generally performed using a Bayesian approach. The 91-GHz channel provides the highest spatial resolution (12.5 km $\times$ 12.5 km), and the other channels are used to compensate atmospheric factors, as was done with the AMSR2 data. The retrieval algorithm is also based on the polarization difference between the V and H channels. However, in this algorithm, the other channels are used in the model, besides for quality assessment, resulting in a smoother transition between the open water and SIC larger than 80%. The SIC maps[3] used as a ground truth for the analysis developed along this paper are obtained from [45]. The OSISAF data set provides other information apart from the SIC maps, such as the sea ice edge and the ice type. In order to develop those products, data from Advanced SCATterometer are also used. Apart from all those combination algorithms, the OSISAF data set provides some quality flags that characterize the quality of the SIC retrievals. In this paper, a minimum confidence data level of 3 is required, as specified in [2]. Lower confidence levels mean that the retrieval is either unreliable, erroneous, or unprocessed.

V. Sea Ice Monitoring Using the U.K. TDS-1 Data

As seen experimentally, the similarity of the received GNSS-R waveform to the coherent model is an indicator of the sea ice presence. In order to assess the performance of the proposed estimators, some intermediate steps have been performed to the GNSS-R data. First, all the available U.K. TDS-1 data with a latitude larger than 50° for the Northern Hemisphere, and lower than −50° for the Southern Hemisphere have been used. The temporal range of that data set includes the following dates: October 31, 2014, October 8, 2014, October 15–17, 2014, October 23, 2014, January 26–28, 2015, February 3–5, 2015, February 11–13, 2015, and February 19–21, 2015. Note that there is a gap in the GNSS-R data between November 23, 2014 and January 26, 2015, because there was a Christmas break, and orbital parameters were corrupted [46]. For that data set, only those DDMs with a thermal SNR larger than 0 dB were used, since lower SNR indicates that the DDMs do not have good quality. In a previous analysis of the U.K. TDS-1 data, this parameter was even more restrictive (3-dB minimum SNR required) [30]. However, as both the U.K. TDS-1 orbit and GPS constellation were not designed to monitor polar areas, it was decided to lower this constrain as otherwise the data set becomes very limited.

Regarding the ground-truth data, they have been split in Arctic and Antarctic regions, and the two different ground-truth data sets used, which leads to four different analyses. Also, a pixel has been considered as an ice pixel if the SIC value is larger than 15% [42], [43]. The pixel correspondence between the GNSS-R data and the ground truth has been performed by a minimum distance algorithm between the

[3]The same as OSISAF maps, but using a grid resolution of 10 km.

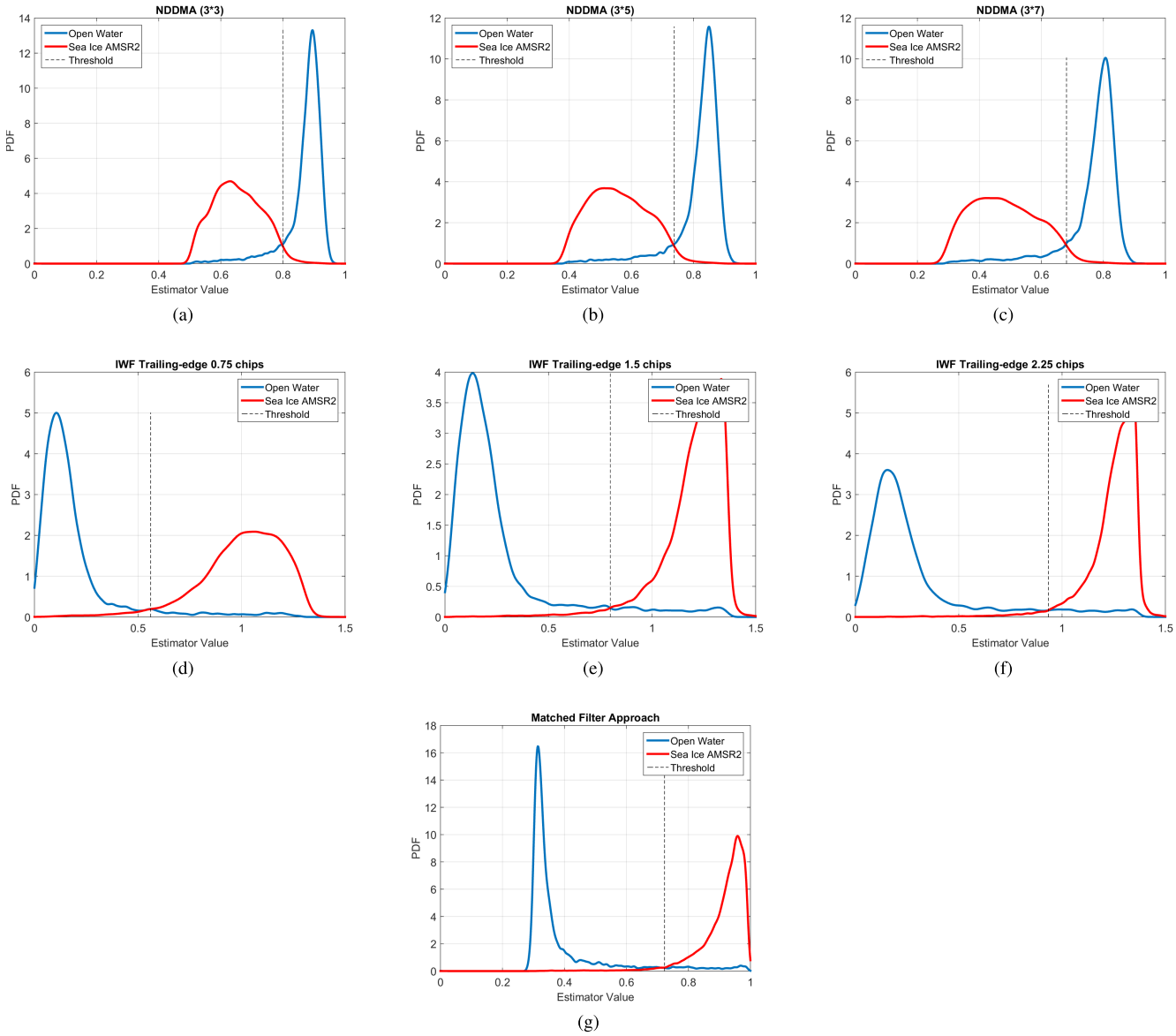

Fig. 2. Estimators' performance for the Northern Hemisphere using the AMSR2 data set. (a) Normalized DDMA 3×3. (b) Normalized DDMA 3×5. (c) Normalized DDMA 3×7. (d) TES 750 ns. (e) TES 1.5 μs. (f) TES 2.25 μs. (g) Matched filter.

geolocated GNSS-R data and the ground-truth grid. A land mask was applied to avoid land contaminated pixels on the data analysis.

A. Performance Evaluation of the Estimators Proposed

Taking into account the previous assumptions, the sea ice detection performance for the different proposed estimators has been evaluated through a Bayesian approach. The pdf of the estimator value for the ice pixels and for the open water pixels was computed and the threshold to determine the presence of ice was chosen using a maximum likelihood criterion, assuming there was no *a priori* information about the pixels' content [47]. This means that the probability of having an ice pixel or an open water pixel, in the entire data set, is assumed to be equal. Fig. 2 shows the pdf of the estimators proposed for the Northern Hemisphere using the AMSR2 data set as ground truth. Fig. 2(a)–(c) shows the performance of the DDMA algorithm for the three different approaches selected, using three Doppler bins and three, five, and seven delay bins. As seen, the three of them look similar, and as the delay bins used increase, the threshold decreases. What occurs with this algorithm is that the smaller the average computed is, the more similar to the WAF the reflected signal is. If the reflection is incoherent, then the reflected signal does not drop so quickly and the normalized DDMA increases. Fig. 2(d)–(f) shows the performance of the TES algorithm. In this case, the sharper the slope, the more similar to the Doppler cut of the WAF the DIW is. Consequently, ice values appear on the right, whereas with the DDMA they appear on the left. Qualitatively, this estimator seems to perform better than the DDMA in each of its three different versions. Finally, the matched filter approach is shown in Fig. 2(g). Herein, it is possible to see that the pdf looks narrower and sharper than with previous estimators. Qualitatively, it seems to be the best estimator to distinguish between sea ice and open water.

TABLE I

PERFORMANCE EVALUATION OF THE ESTIMATORS PROPOSED FOR ARCTIC AND ANTARCTIC REGIONS AS A FUNCTION OF THE TWO DIFFERENT GROUND TRUTHS USED, THE OSISAF AND THE ASI AMSR2 DATA SETS

		Arctic				**Antarctic**			
	Estimators	Pd	Pfa	Pe	Th.	Pd	Pfa	Pe	Th.
OSISAF	NDDMA (3*3)	0.9822	0.0633	0.0401	0.802	0.9792	0.1254	0.0726	0.805
	NDDMA (3*5)	0.9794	0.0659	0.0428	0.739	0.9796	0.1261	0.0729	0.742
	NDDMA (3*7)	0.9749	0.0732	0.0487	0.682	0.9801	0.1323	0.0758	0.688
	TE (0.75 CA Chips)	0.9827	0.0351	0.0262	0.534	0.9810	0.1022	0.0605	0.495
	TE (1.5 CA Chips)	0.9853	0.0374	0.0260	0.795	0.9808	0.0997	0.0594	0.765
	TE (2.25 CA Chips)	0.9824	0.0383	0.0279	0.936	0.9830	0.1019	0.0594	0.825
	MF	0.9869	0.0379	0.0254	0.707	0.9803	0.0972	0.0583	0.668
ASI AMSR2	NDDMA (3*3)	0.9745	0.1347	0.0795	0.798	0.9756	0.1745	0.0990	0.808
	NDDMA (3*5)	0.9753	0.1384	0.0811	0.737	0.9758	0.1741	0.0988	0.744
	NDDMA (3*7)	0.9726	0.1464	0.0864	0.681	0.9755	0.1789	0.1013	0.688
	TE (0.75 CA Chips)	0.9678	0.0886	0.06	0.577	0.9755	0.1529	0.0886	0.454
	TE (1.5 CA Chips)	0.9764	0.1018	0.0626	0.804	0.9733	0.1488	0.0877	0.737
	TE (2.25 CA Chips)	0.9744	0.1015	0.0635	0.942	0.9808	0.1579	0.0885	0.782
	MF	0.9764	0.0985	0.0609	0.725	0.9748	0.1506	0.0878	0.642

The same operation has been performed for the OSISAF data set, and for both ground truths over the Antarctic region. The pdfs obtained are similar to the ones presented in Fig. 2, indicating a similar behavior. This shows that the algorithms performed in the same way independently of the data origin. Table I summarizes the results obtained and evaluates quantitatively the performance of all the estimators proposed. Therein, four parameters are computed for each ground truth available (OSISAF and ASI AMSR2), and each region (Arctic and Antarctic): the probability of detection (Pd), the probability of false alarm (Pfa), the probability of error (Pe), and the threshold selected [47].

In general, it is possible to see that, independently of the algorithm used, for any region and any ground-truth data set, the probability of detecting sea ice when there is sea ice is larger than 97%, reaching larger values for the OSISAF ground truth. For the ASI data set, the Pd is lower and the Pfa is larger, which indicates that the selected approach is more similar to the OSISAF ground truth. Note that the estimators with the worst performance, which is evaluated by the Pe, are the ones based on the DDMA. However, those are more consistent and independent of the ground truth and the region observed, as they all have a similar threshold. This occurs because the threshold is determined by the shape of the pdfs, and for those estimators, they are closer, and the slopes around the threshold are larger. On the other hand, the threshold for the other estimators is not as consistent. Looking to the pdfs presented in Fig. 2, they are more separated than for the DDMA, and the slopes around the threshold are smaller. This means that the threshold selection is not very important, and the Pd and Pfa values will not change much by changing the computed threshold. Also, note that the performance of the trailing edge estimators and the matched filter approach is similar. However, the matched filter approach seems to be less sensitive to the threshold selection just by qualitatively exploring the pdfs. It is also the simplest one to be implemented, since it only requires one fast Fourier transform (FFT) and one inverse fast Fourier transform. For this reason, it is the preferred approach, as it can be easily implemented in a real-time processing software onboard the satellite, without the need of further algorithm intelligence such as peak retracking. Finally, it is also worth mentioning why the results obtained are more similar to the OSISAF data set than to the ASI algorithm over the AMSR2 data set, which occurs because the OSISAF uses a combination of different frequency bands which are closer to the L-band, whereas the ASI algorithm uses only the 90-GHz band, being sensitive at some points to different parameter scales. The fact that the OSISAF data set has a quality flag that evaluates and specifies, which values are reliable, also helps to obtain better results with the OSISAF ground truth.

B. SIC Maps From Ground Truth and GNSS-R Data

Fig. 3 shows the sea ice detection maps created from the GNSS-R data using the matched filter approach together with the SIC maps from the two ground truths available for both the Arctic and Antarctic regions. Note that February 15, 2015 is the middle of the winter in the Northern Hemisphere and the middle of the summer in the Southern Hemisphere, which is why the North Pole has more sea ice than the South Pole. In all the maps, the presence of ice is shown by purple whereas the presence of open water is shown by the light blue, which correspond to the colorbar on the right of the figures. The gaps in the GNSS-R transects are due to DDMs with a thermal SNR lower than 0 dB or land contaminated pixels. Also, as aforementioned, in the OSISAF maps, there might be gaps in the case of unreliable retrievals. The SIC values from OSISAF and ASI AMSR2 are scaled from 0% to 100%, with the 0% the dark blue and the 100% the bright yellow, which correspond to the colorbar on the left of the figures. The coordinate system used to represent those maps is the polar stereographic coordinate system. Therein, it is seen how the transitions between open water and sea ice are monitored, and the change observed is very drastic, as expected from the pdfs. The sea ice edge seems to be accurately detected using the GNSS-R data (see Fig. 5). Based on the specular reflection theory, assuming coherent reflection for the sea ice regions and using the TDS-1 satellite parameters, the spatial resolution is $\sim$6 km $\times$ 0.4 km (400 m $\times$ 400 m for 1 ms of coherent

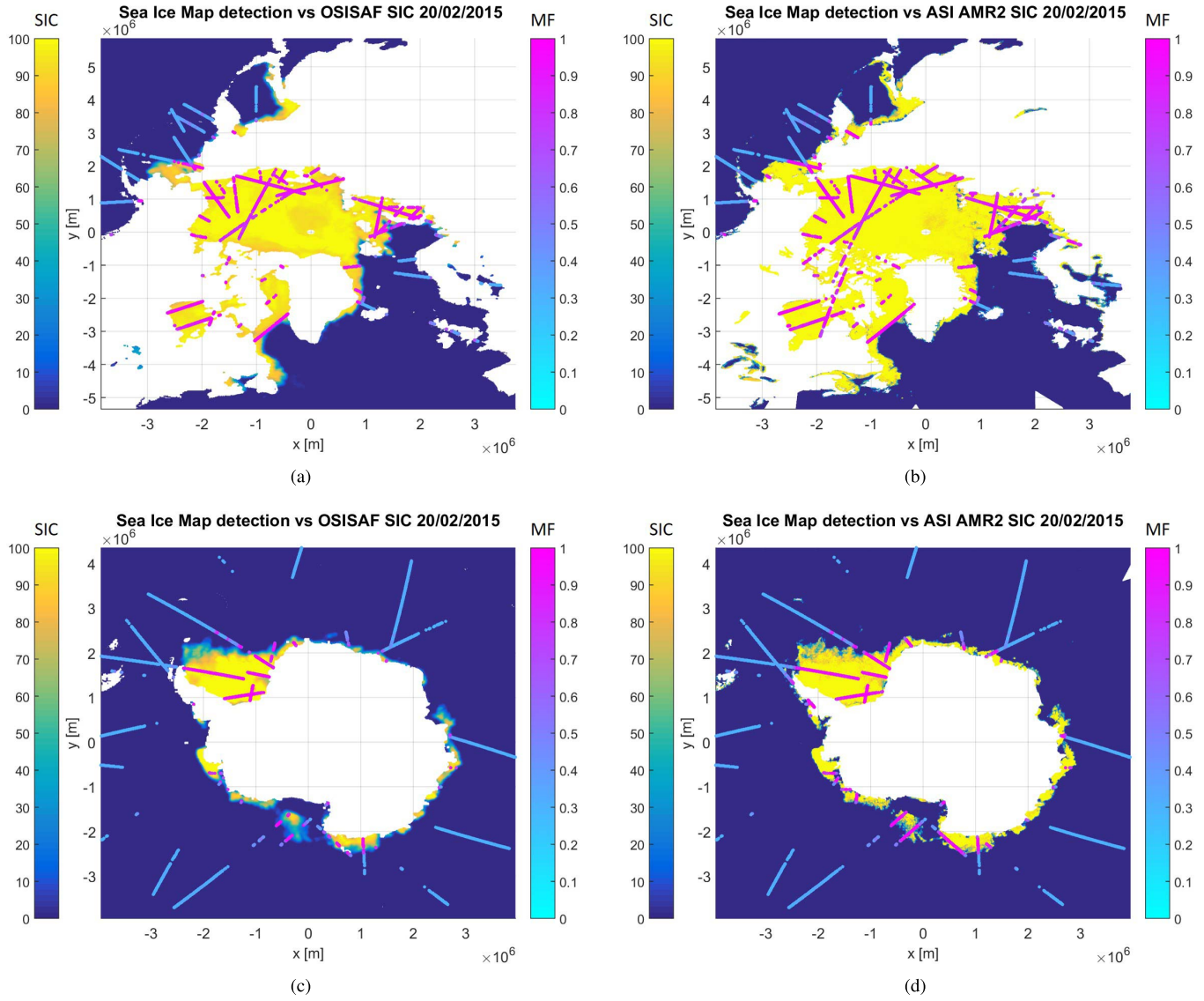

Fig. 3. SIC Maps of February 20, 2015 from OSISAF and ASI AMSR2 of the Northern and Southern Hemisphere overlaid with the matched filter GNSS-R approach. (a) Arctic OSISAF. (b) Arctic ASI AMSR2. (c) Antarctic OSISAF. (d) Antarctic ASI AMSR2.

integration time blurred to 6 km × 400 m due to the 1 s of incoherent integration time), which is half of the SSMIS pixel in the along-track direction.

Furthermore, note that GNSS-R data look like different transects. This is one of the properties of the multistatic GNSS-R techniques. Instead of being an image like a SAR or a microwave radiometer, it is a collection of transects with all the satellites in view. In order to generate a map with GNSS-R data, interpolation is required. Herein, the interpolation approach has not been performed as the mission specifications do not allow one to obtain sufficient points to generate a reliable map. However, a GNSS-R mission with the appropriate specifications to monitor the polar regions, such as the one simulated in [25], would provide enough quality data to generate polar images.

Fig. 4 shows a similar image to Fig. 3, but in this case for November 15, 2014. Herein, the Arctic regions are less frozen than for February, 2015 as the freezing period has just started, whereas the Antarctic regions have a larger amount of sea ice because the melting process is just starting. Again, the transitions are monitored by the GNSS-R data. Note that in the Antarctic, there is an area close to the coast that melted before the outer ice layer, and it is detected by the GNSS-R data. Also, note that for the 2014 images, there is much less GNSS-R data available because they come from the beginning of the mission, whereas the 2015 ones come from a more consolidated period of the mission.

Finally, in order to show the performance of the algorithm at a higher resolution, Fig. 5 is added. Fig. 5(a) and (b) represent a zoomed-in-view area on the Arctic region, whereas Fig. 5(c) and (d) represent a zoomed-in-view area on the Antarctic region. It can also be seen how the resolution of the SIC from the ASI algorithm is higher than the one from the OSISAF, the images of which are more blurred. Recall that ASI uses one single frequency to estimate SIC, whereas the OSISAF algorithm uses a combination of frequencies resulting in smooth transitions or this blurring effect. Note that there are some missing points on the GNSS-R data set in the OSISAF

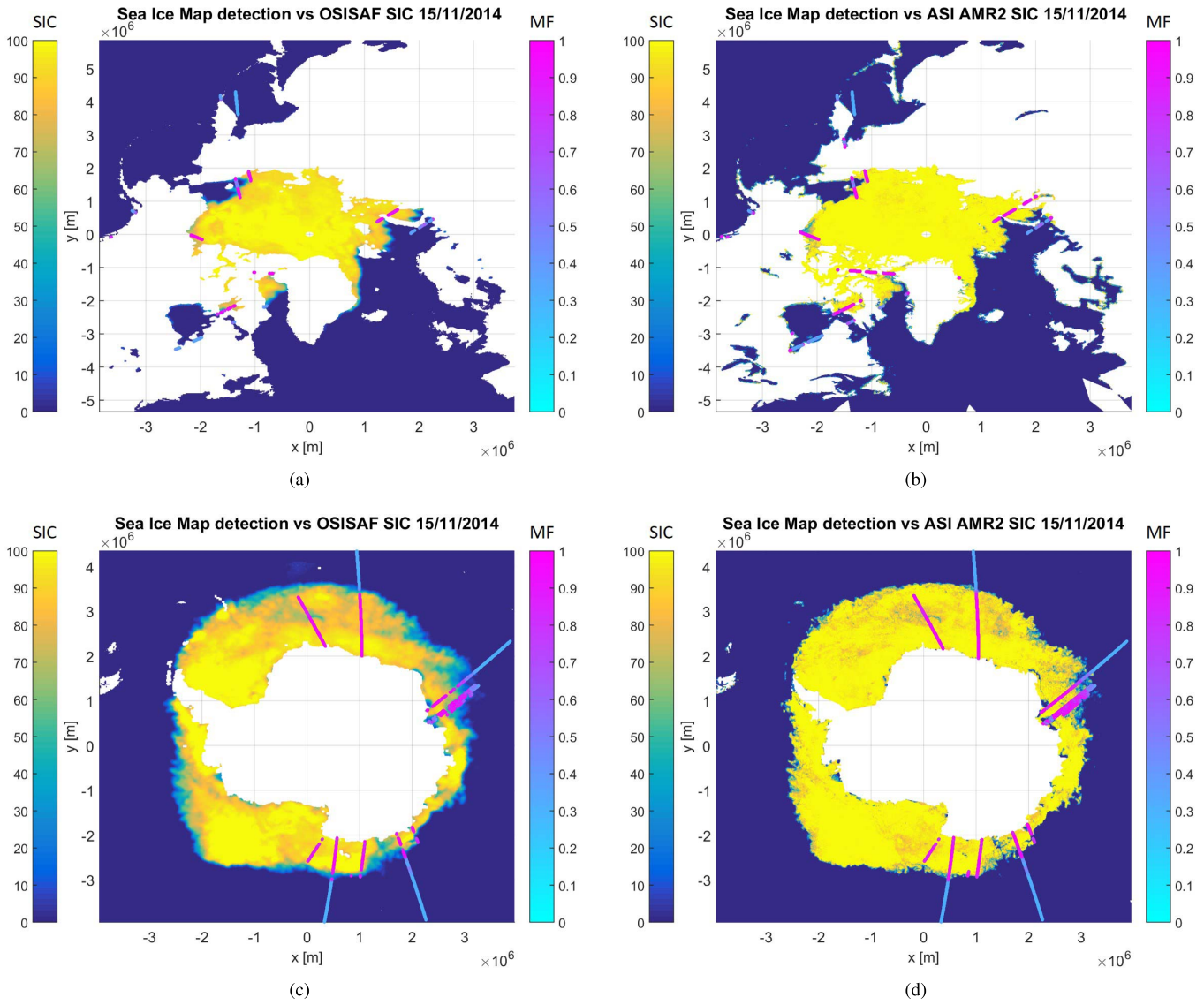

Fig. 4. SIC Maps of November 15, 2014 from OSISAF and ASI AMSR2 of the Northern and Southern Hemisphere overlaid with the matched filter GNSS-R approach. (a) Arctic OSISAF. (b) Arctic ASI AMSR2. (c) Antarctic OSISAF. (d) Antarctic ASI AMSR2.

maps in comparison to the ASI maps and this occurs, because the SIC value from the OSISAF map was determined as unreliable. If the SIC value was unreliable, the GNSS-R data are not plotted. No quality flag was available from the ASI maps, so only the GNSS-R SNR data filtering is affecting those maps.

VI. Discussion

A sea ice detection algorithm has been presented based on the sea ice scattering models available in the literature. Several estimators have been proposed to detect the presence of sea ice and their performance have been evaluated through a Bayesian approach. Sea ice maps from the different ground truths available have been shown with the GNSS-R matched filter approach overlaying them. Furthermore, it has been attempted to go deeper and determine if the coherent GNSS-R waveform was sensitive to other parameters apart from the sea ice presence, and therefore if it could be used, for instance, for sea ice classification (first-year, multiyear, or pure ice [48]). By looking at the maps provided, it is seen that the detection parameter is not sensitive to sea ice type, which might occur due to the roughness scale at L-band. On the one hand, following the ice scattering coherent model, one would expect to find the largest power received when there is thin ice, since the water is freezing and calm (a property of new ice formation [15]), and water has a very large dielectric constant. When the SIC increases, the equivalent dielectric constant is a mixture of the ice one and water one, and as the dielectric constant of ice is much smaller than the water one, the equivalent dielectric constant decreases and, therefore, so does the reflected power or the reflected SNR. This means that in the limit, when the SIC is 100%, the coherent model would work, but with a lower echo received. The same reasoning applies to first-year ice, the dielectric constant of which is larger than that of multiyear ice, which in its turn has the dielectric constant larger than that for the pure ice. On the other hand, no correlation was found between the SNR received and the SIC. This might be interpreted as GNSS-R not being sensitive to the SIC, but one must take

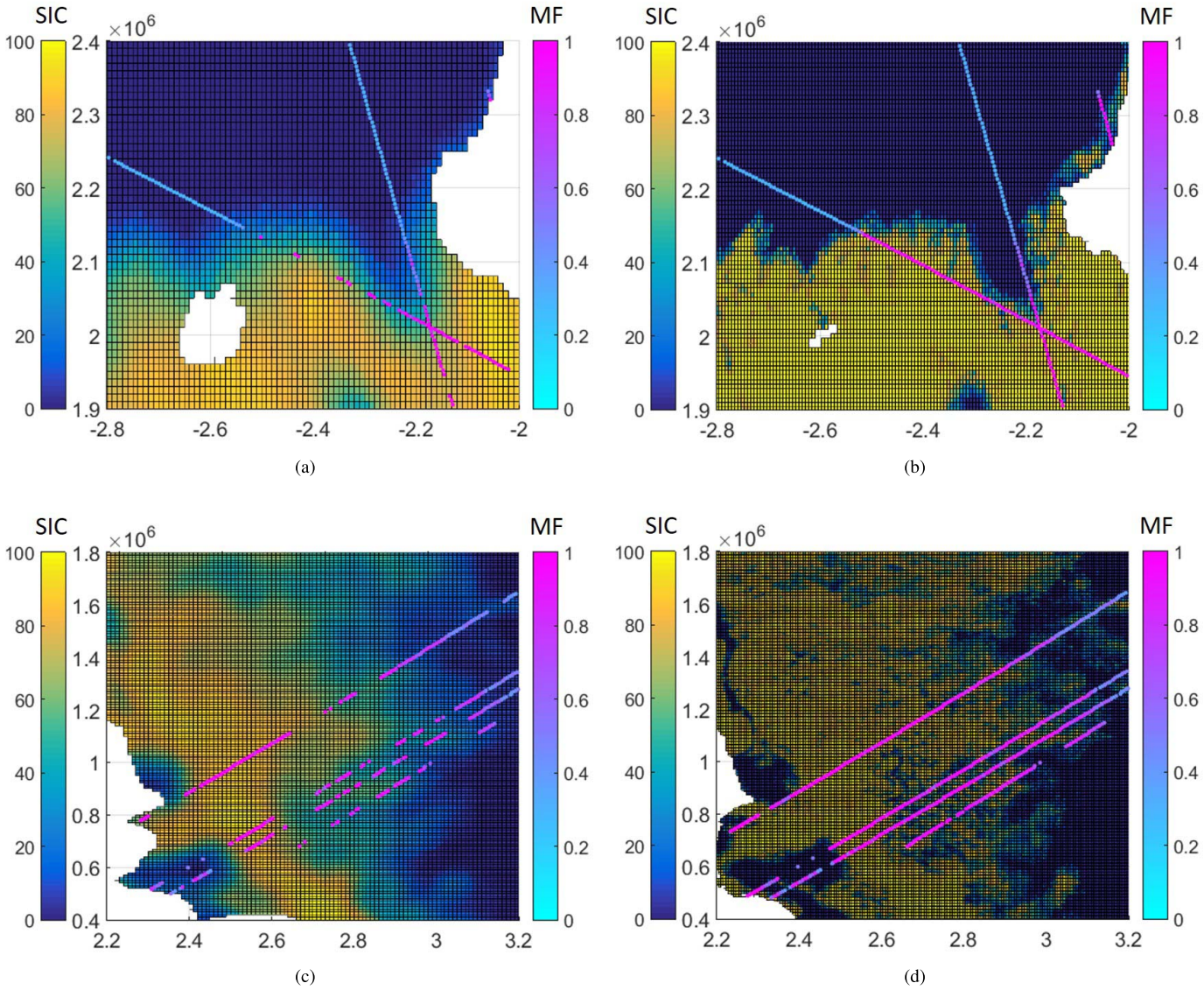

Fig. 5. Zoomed-in view of SIC Maps of February 20, 2015 for the Arctic data and from November 15, 2014 for the Antarctic data, for both OSISAF and ASI AMSR2 ground truth overlaying the matched filter GNSS-R approach. (a) Arctic OSISAF. (b) Arctic ASI AMSR2. (c) Antarctic OSISAF. (d) Antarctic ASI AMSR2.

into account that the U.K. TDS-1 data were not calibrated. Therefore, having a mixture of data from different satellites prevents the extraction of any robust conclusion from the data set used. This relation should be explored in the future with calibrated data. However, different roughness scales may apply to this analysis, making it more difficult to obtain a clear relationship. This is extremely important because a similar problem to the soil moisture retrieval from scatterometric data is faced, since both roughness and dielectric constant affect the back-scattered power, and calibration would not be a solution. CYGNSS mission will provide calibrated data, but its orbit, which was selected to monitor tropical cyclones, will preclude picking reflections from sea ice. In order to test this hypothesis, data from the forthcoming European Space Agency Global Navigation Satellite Systems (GNSS) rEflectometry, Radio Occultation and Scatterometry (GEROS) mission will be needed. National Aeronautics and Space Administration may consider a CYGNSS follow-on mission, and new scientific challenges, such as the SIC monitoring, could be one of its goals.

The methodology to detect the presence of sea is based on on estimating the similarity to the coherent waveform. When it is coherent, the ground resolution of the GNSS-R data corresponds to the first Fresnel zone [49], [50], which is approximately 400 m $\times$ 400 m for a satellite at 650-km altitude. Taking into account the satellite's speed (6 km/s) and 1 s of noncoherent integration, this leads to a final ground resolution of approximately 6 km $\times$ 0.4 km. This resolution is similar to the one achieved by microwave radiometers working at 90 GHz, in the along-track direction, and much better in the across-track direction. This is a major point regarding this technique, since technology is much cheaper at L-band than at 90 GHz, and L-band is much less sensitive to atmospheric effects than the 90-GHz frequency band [51] requiring less corrections. However, when the reflection is produced over rough water, the spatial resolution is largely

degraded, as the reflection is mostly incoherent. Spatial resolution of coherently scattered GNSS signals is much better than microwave radiometers working at the same frequency band (L-band), such as the Soil Moisture Ocean Salinity (SMOS), the Aquarius, and the Soil Moisture Active and Passive (SMAP) radiometers.

One disadvantage of the GNSS-R approach that is worth mentioning is that, currently, due to the dearth of available satellite data, the product derived contains much less information than the one derived from the conventional radiometric data. Therefore, currently, the sea ice product derived from the GNSS-R is not competitive enough in comparison to the radiometric one. However, the planned launch of new GNSS-R satellite constellations and the rise of available GNSS satellites would help to cover this gap and, therefore, generate a product with the same spatial resolution and the same coverage than the higher frequency passive techniques, at a fraction of their cost.

One aspect that has not yet been discussed is the Pfa obtained by all the estimators, and the reasons why a false alarm may be produced. The sea ice presence is determined by the similarity to the WAF, which means that the reflected surface must be flat. In several of the data sets used, it has been noticed that close to the sea ice edges the GNSS-R data were detecting ice presence, whereas the ground truth had not yet detected ice. The ground-truth data used are SIC maps averaging several images of several radiometer orbits passes, and each pixel data is not time referenced. However, GNSS-R data are time referenced. Several continuous data observations showed that when ice was detected close to the ice edges by the GNSS-R technique, but not with the radiometric data, the following day it was detected as an ice pixel by the radiometric data. This indicates that either the OSISAF data or the AMSR2 data were obtained hours before the GNSS-R data, or that in the freezing process (new ice formation), the sea becomes calmer before freezing, and the proposed GNSS-R technique detects sea ice also when sea becomes calmer (coherent reflection).

The performance of the sea ice classification algorithm was tested when the SIC was only 1% for a sensitivity study. The algorithms performed better in that case which is in line with the coherent detection methodology, since even for a 1% SIC, the reflection is mostly coherent [43]. However, traditionally, sea ice pixels were considered when at least 15% SIC was detected. Therefore, this is the criterion that has been followed in this paper.

VII. Conclusion

This paper has presented a methodology to monitor and detect sea ice presence over the Arctic and Antarctic regions using the U.K. TDS-1 GNSS-R data. The detection is based on the similarity of the measured DIW or DDM to the coherent one, as when the reflection occurs over a sea ice region, the scattering is mostly coherent, whereas when it occurs over open ocean, it follows the incoherent model. Three different estimators with different properties are used along this paper for the sea ice detection: the normalized DDMA, the TES, and the matched filter approach. Among them, the matched filter approach is preferred as it classifies with only one value between 0 and 1 if it is an ice pixel or an open ocean pixel. Furthermore, it is the one that requires less computational cost and it can be implemented easily on the on-board processing. In order to assess the validity of the algorithms proposed, two different ground-truth data sets have been used: the OSISAF data set and the ASI algorithm over AMSR2 data. The best results are obtained for both, the TES in its three versions and the matched filter estimator, over the Arctic region and using the OSISAF data set as ground truth, obtaining a Pd of 98% and a Pe of approximately 2.5%.

The relation between the reflected power and the SIC could not be evaluated with the appropriate degree of accuracy as the U.K. TDS-1 GNSS-R data lacked of the measurement of the direct signal, which avoids obtaining calibrated measurements. This means that only relative measurements as the ones presented can be used. However, the results from this paper are encouraging for future GNSS-R missions, since this GNSS-R technique is more cost effective and has the same ground resolution than microwave radiometers at 90 GHz, and it is less prone to atmospheric influence. Currently available GNSS-R data show much less coverage than passive microwave sea ice data, but future missions will help to evaluate how competitive this technique can be in comparison to the traditional ones. Unfortunately, the CYGNSS mission that will be launched in 2016 will not be able to test these algorithms due to its orbit inclination (35°), but other forthcoming GNSS-R missions, such as GEROS or a potential CYGNSS follow-on mission, will be able to.

Acknowledgment

SIC data from September 1, 2014 to February 22, 2015 were obtained from http://www.meereisportal.de under Grant REKLIM-2013-04 (ASI AMSR2 data). The SIC product is from the EUMETSAT OSISAF. Ice concentration is computed from atmospherically corrected SSMIS brightness temperatures, using a combination of the state-of-the-art algorithms. It has been operational since 2005. SIC data from September 1, 2014 to February 22, 2015 were obtained from http://osisaf.met.no/p/ice/ (OSISAF SSMIS data). The authors would like to thank SSTL and the Measurement of earth Reflected Radio-navigation Signals By Satellite Project for the U.K. TDS-1 data provided to conduct this research at no cost. They would also like to thank S. Gleason for interesting discussions about how to process TDS-1 data. They would also like to thank C. Gabarro for sea ice detection discussion and for providing some processed SMOS data that could be used together with TDS-1 data for Sea Ice Mapping.

References

[1] G. Spreen, L. Kaleschke, and G. Heygster, "Sea ice remote sensing using AMSR-E 89-GHz channels," *J. Geophys. Res.*, vol. 113, no. C2, p. C02S03, Jan. 2008. [Online]. Available: http://doi.wiley.com/10.1029/2005JC003384

[2] S. Andersen *et al.*, "Ocean & sea ice SAF: Sea ice product user's manual, OSI-401-a, OSI-402-a, OSI-403-a," Meteo France, Ifremer, EUMETSAT, DMI, Norwegian Meteorol. Inst., Darmstadt, Germany, Tech. Rep., 2014.

[3] C. Rapley *et al.*, "A study of satellite radar altimeter operations over ice-covered surfaces," Univ. College London, London, U.K., Tech. Rep. ESA CR 5182/82/F/CG(SC), 1983.

[4] P. Beckmann and A. Spizzichino, *The Scattering of Electromagnetic Waves from Rough Surfaces* (Artech House Radar Library). Artech Print on Demand, 1987.

[5] C. D. Hall and R. A. Cordey, "Multistatic scatterometry," in *Proc. IEEE Int. Geosci. Remote Sens. Symp., Remote Sens. Moving Toward 21st Century*, Sep. 1988, pp. 561–562. [Online]. Available: http://ieeexplore.ieee.org/lpdocs/epic03/wrapper.htm?arnumber=570200

[6] M. Martín-Neira, "A passive reflectometry and interferometry system (PARIS): Application to ocean altimetry," *ESA J.*, vol. 17, no. 4, pp. 331–355, 1993. [Online]. Available: http://xenon.colorado.edu/spotlight/kb/gps_reflections/Martin-Neira-PARIS-1993.pdf

[7] M. Martín-Neira, M. Caparrini, J. Font-Rossello, S. Lannelongue, and C. S. Vallmitjana, "The PARIS concept: An experimental demonstration of sea surface altimetry using GPS reflected signals," *IEEE Trans. Geosci. Remote Sens.*, vol. 39, no. 1, pp. 142–150, Jan. 2001. [Online]. Available: http://ieeexplore.ieee.org/lpdocs/epic03/wrapper.htm?arnumber=898676

[8] M. Martín-Neira, S. D'Addio, C. Buck, N. Floury, and R. Prieto-Cerdeira, "The PARIS ocean altimeter in-orbit demonstrator," *IEEE Trans. Geosci. Remote Sens.*, vol. 49, no. 6, pp. 2209–2237, Jun. 2011. [Online]. Available: http://ieeexplore.ieee.org/lpdocs/epic03/wrapper.htm?arnumber=5682027

[9] A. Komjathy, J. Maslanik, V. U. Zavorotny, P. Axelrad, and S. J. Katzberg, "Sea ice remote sensing using surface reflected GPS signals," in *Proc. IEEE Int. Geosci. Remote Sens. Symp. (IGARSS), Taking Pulse Planet, Role Remote Sens. Manag. Environ. (Cat. No.00CH37120)*, vol. 7. Jul. 2000, pp. 2855–2857. [Online]. Available: http://ieeexplore.ieee.org/lpdocs/epic03/wrapper.htm?arnumber=860270

[10] M. Wiehl, B. Legrésy, and R. Dietrich, "Potential of reflected GNSS signals for ice sheet remote sensing," *Prog. Electromagn. Res.*, vol. 40, pp. 177–205, 2003. [Online]. Available: http://www.jpier.org/PIER/pier.php?paper=0210222

[11] S. Gleason, "Remote sensing of ocean, ice and land surfaces using bistatically scattered GNSS signals from low earth orbit," Ph.D. dissertation, Univ. Surrey, Guildford, U.K., 2006.

[12] S. Gleason, "Towards sea ice remote sensing with space detected GPS signals: Demonstration of technical feasibility and initial consistency check using low resolution sea ice information," *Remote Sens.*, vol. 2, no. 8, pp. 2017–2039, Aug. 2010. [Online]. Available: http://www.mdpi.com/2072-4292/2/8/2017/

[13] M. B. Rivas, J. A. Maslanik, and P. Axelrad, "Bistatic scattering of GPS signals off arctic sea ice," *IEEE Trans. Geosci. Remote Sens.*, vol. 48, no. 3, pp. 1548–1553, Mar. 2010. [Online]. Available: http://ieeexplore.ieee.org/lpdocs/epic03/wrapper.htm?arnumber=5256254

[14] G. S. Brown, "The average impulse response of a rough surface and its applications," *IEEE Trans. Antennas Propag.*, vol. 25, no. 1, pp. 67–74, Jan. 1977. [Online]. Available: http://ieeexplore.ieee.org/lpdocs/epic03/wrapper.htm?arnumber=1141536

[15] G. S. Brown, "A theory for near-normal incidence microwave scattering from first-year sea ice," *Radio Sci.*, vol. 17, no. 1, pp. 233–243, Jan. 1982. [Online]. Available: http://doi.wiley.com/10.1029/RS017i001p00233

[16] C. Rapley *et al.*, "Applications and scientific uses of ERS-1 radar altimeter data," Univ. College London, London, U.K., Tech. Rep. ESA CR 5684/83/NL/BI, 1985.

[17] M. R. Drinkwater, "K_u band airborne radar altimeter observations of marginal sea ice during the 1984 Marginal Ice Zone Experiment," *J. Geophys. Res.*, vol. 96, no. C3, pp. 4555–4572, 1991. [Online]. Available: http://doi.wiley.com/10.1029/90JC01954

[18] P. M. Woodward, "Radar ambiguity analysis," Tech. Note 731, 1967.

[19] V. U. Zavorotny and A. G. Voronovich, "Scattering of GPS signals from the ocean with wind remote sensing application," *IEEE Trans. Geosci. Remote Sens.*, vol. 38, no. 2, pp. 951–964, Mar. 2000. [Online]. Available: http://ieeexplore.ieee.org/lpdocs/epic03/wrapper.htm?arnumber=841977

[20] T. Elfouhaily, D. R. Thompson, and L. Linstrom, "Delay-Doppler analysis of bistatically reflected signals from the ocean surface: Theory and application," *IEEE Trans. Geosci. Remote Sens.*, vol. 40, no. 3, pp. 560–573, Mar. 2002. [Online]. Available: http://ieeexplore.ieee.org/lpdocs/epic03/wrapper.htm?arnumber=1000316

[21] J. F. Marchan-Hernandez, A. Camps, N. Rodriguez-Alvarez, E. Valencia, X. Bosch-Lluis, and I. Ramos-Perez, "An efficient algorithm to the simulation of delay–Doppler maps of reflected global navigation satellite system signals," *IEEE Trans. Geosci. Remote Sens.*, vol. 47, no. 8, pp. 2733–2740, Aug. 2009. [Online]. Available: http://ieeexplore.ieee.org/lpdocs/epic03/wrapper.htm?arnumber=4813235

[22] D. Pascual, A. Camps, F. Martin, H. Park, A. A. Arroyo, and R. Onrubia, "Precision bounds in GNSS-R ocean altimetry," *IEEE J. Sel. Topics Appl. Earth Observ. Remote Sens.*, vol. 7, no. 5, pp. 1416–1423, May 2014. [Online]. Available: http://ieeexplore.ieee.org/lpdocs/epic03/wrapper.htm?arnumber=6742726

[23] D. P. Winebrenner *et al.*, "Microwave sea ice signature modeling," in *Microwave Remote Sensing of Sea Ice*. Hoboken, NJ, USA: Wiley, 1992, pp. 137–175. [Online]. Available: http://doi.wiley.com/10.1029/GM068p0137

[24] D. G. Barber *et al.*, "The role of snow on microwave emission and scattering over first-year sea ice," *IEEE Trans. Geosci. Remote Sens.*, vol. 36, no. 5, pp. 1750–1763, Sep. 1998. [Online]. Available: http://ieeexplore.ieee.org/document/718643/

[25] V. U. Zavorotny, S. Gleason, E. Cardellach, and A. Camps, "Tutorial on remote sensing using GNSS bistatic radar of opportunity," *IEEE Geosci. Remote Sens. Mag.*, vol. 2, no. 4, pp. 8–45, Dec. 2014. [Online]. Available: http://ieeexplore.ieee.org/lpdocs/epic03/wrapper.htm?arnumber=6985926

[26] R. D. De Roo and F. T. Ulaby, "Bistatic specular scattering from rough dielectric surfaces," *IEEE Trans. Antennas Propag.*, vol. 42, no. 2, pp. 220–231, Feb. 1994. [Online]. Available: http://ieeexplore.ieee.org/lpdocs/epic03/wrapper.htm?arnumber=277216

[27] T. W. K. Armitage and M. W. J. Davidson, "Using the interferometric capabilities of the ESA CryoSat-2 mission to improve the accuracy of sea ice freeboard retrievals," *IEEE Trans. Geosci. Remote Sens.*, vol. 52, no. 1, pp. 529–536, Jan. 2014. [Online]. Available: http://ieeexplore.ieee.org/lpdocs/epic03/wrapper.htm?arnumber=6479282

[28] J. L. Garrison, A. Komjathy, V. U. Zavorotny, and S. J. Katzberg, "Wind speed measurement using forward scattered GPS signals," *IEEE Trans. Geosci. Remote Sens.*, vol. 40, no. 1, pp. 50–65, Jan. 2002. [Online]. Available: http://ieeexplore.ieee.org/lpdocs/epic03/wrapper.htm?arnumber=981349

[29] S. Gleason *et al.*, "Detection and Processing of bistatically reflected GPS signals from low earth orbit for the purpose of ocean remote sensing," *IEEE Trans. Geosci. Remote Sens.*, vol. 43, no. 6, pp. 1229–1241, Jun. 2005. [Online]. Available: http://ieeexplore.ieee.org/lpdocs/epic03/wrapper.htm?arnumber=1433022

[30] G. Foti *et al.*, "Spaceborne GNSS reflectometry for ocean winds: First results from the UK TechDemoSat-1 mission," *Geophys. Res. Lett.*, vol. 42, no. 13, pp. 5435–5441, Jul. 2015. [Online]. Available: http://doi.wiley.com/10.1002/2015GL064204

[31] N. Pierdicca, L. Guerriero, R. Giusto, M. Brogioni, and A. Egido, "SAVERS: A simulator of GNSS reflections from bare and vegetated soils," *IEEE Trans. Geosci. Remote Sens.*, vol. 52, no. 10, pp. 6542–6554, Oct. 2014. [Online]. Available: http://ieeexplore.ieee.org/lpdocs/epic03/wrapper.htm?arnumber=6725659

[32] A. Fung and H. Eom, "Coherent scattering of a spherical wave from an irregular surface," *IEEE Trans. Antennas Propag.*, vol. 31, no. 1, pp. 68–72, Jan. 1983.

[33] F. T. Ulaby and D. G. Long, "Coherent and non-coherent scattering," in *Microwave Radar and Radiometric Remote Sensing*. Ann Arbor, MI, USA: Artech House, 2014, secs. 5–10, pp. 194–203.

[34] E. Cardellach, G. Ruffini, D. Pino, A. Rius, A. Komjathy, and J. L. Garrison, "Mediterranean Balloon Experiment: Ocean wind speed sensing from the stratosphere, using GPS reflections," *Remote Sens. Environ.*, vol. 88, no. 3, pp. 351–362, Dec. 2003. [Online]. Available: http://linkinghub.elsevier.com/retrieve/pii/S0034425703001767

[35] A. Komjathy, M. Armatys, D. Masters, P. Axelrad, V. Zavorotny, and S. Katzberg, "Retrieval of ocean surface wind speed and wind direction using reflected GPS signals," *J. Atmos. Ocean. Technol.*, vol. 21, no. 3, pp. 515–526, Mar. 2004. [Online]. Available: http://journals.ametsoc.org/doi/abs/10.1175/1520-0426%282004%29021%3C0515%3AROOSWS%3E2.0.CO%3B2

[36] E. Valencia *et al.*, "On the use of GNSS-R data to correct L-band brightness temperatures for sea-state effects: Results of the ALBATROSS field experiments," *IEEE Trans. Geosci. Remote Sens.*, vol. 49, no. 9, pp. 3225–3235, Sep. 2011. [Online]. Available: http://ieeexplore.ieee.org/lpdocs/epic03/wrapper.htm?arnumber=5958602

[37] M. P. Clarizia, C. S. Ruf, P. Jales, and C. Gommenginger, "Spaceborne GNSS-R minimum variance wind speed estimator," *IEEE Trans. Geosci. Remote Sens.*, vol. 52, no. 11, pp. 6829–6843, Nov. 2014. [Online]. Available: http://ieeexplore.ieee.org/lpdocs/epic03/wrapper.htm?arnumber=6744608

[38] M. P. Clarizia, C. S. Ruf, A. O'Brien, and S. Gleason, "A level 2 wind speed retrieval algorithm for the CYGNSS mission," in *Proc. EGU General Assembly Conf. Abstracts*, Vienna, Austria, 2014, Art. no. 15776. [Online]. Available: http://adsabs.harvard.edu/abs/2014EGUGA.1615776C

[39] M. P. Clarizia and C. S. Ruf, "An improved wind speed retrieval algorithm for the CYGNSS mission," in *Proc. AGU Fall Meeting*, San Francisco, CA, USA, 2015. [Online]. Available: https://agu.confex.com/agu/fm15/webprogram/Paper68045.html

[40] F. M. Fetterer, M. R. Drinkwater, K. C. Jezek, S. W. C. Laxon, R. G. Onstott, and L. M. H. Ulander, "Sea ice altimetry," in *Microwave Remote Sensing of Sea Ice* (Geophysical Monograph Series), vol. 68, F. D. Carsey, Ed. Washington, DC, USA: AGU, 1992, pp. 111–135. [Online]. Available: http://doi.wiley.com/10.1029/GM068 and http://doi.wiley.com/10.1029/GM068p0111

[41] S. W. Laxon and C. G. Rapley, "Radar altimeter data quality flagging," *Adv. Space Res.*, vol. 7, no. 11, pp. 315–318, Jan. 1987. [Online]. Available: http://linkinghub.elsevier.com/retrieve/pii/0273117787903322

[42] S. Laxon, "Seasonal and inter-annual variations in Antarctic sea ice extent as mapped by radar altimetry," *Geophys. Res. Lett.*, vol. 17, no. 10, pp. 1553–1556, Sep. 1990. [Online]. Available: http://doi.wiley.com/10.1029/GL017i010p01553

[43] N. R. Peacock and S. W. Laxon, "Sea surface height determination in the Arctic Ocean from ERS altimetry," *J. Geophys. Res.*, vol. 109, no. C7, p. C07001, 2004. [Online]. Available: http://doi.wiley.com/10.1029/2001JC001026

[44] *Sea Ice Concentration Maps From AMSR2 Data*, accessed on May 28, 2017. [Online]. Available: http://www.meereisportal.de

[45] *Ocean & Sea Ice SAF: Sea Ice Concentration Maps*, accessed on May 28, 2017. [Online]. Available: http://osisaf.met.no/p/ice/

[46] P. Jales, "TDS-1 GNSS-R data products & access," in *Proc. TechDemoSat-1 User Consultation Workshop*, 2015.

[47] S. M. Kay, *Fundamentals of Statistical Signal Processing: Detection Theory*, vol. 2, 1st ed. Upper Saddle River, NJ, USA: Prentice-Hall, 1998.

[48] F. T. Ulaby, R. K. Moore, and A. K. Fung, *Microwave Remote Sensing: Active and Passive: Radar Remote Sensing and Surface Scattering and Emission Theory*, vol. 2. 1982.

[49] D. Masters, P. Axelrad, and S. Katzberg, "Initial results of land-reflected GPS bistatic radar measurements in SMEX02," *Remote Sens. Environ.*, vol. 92, no. 4, pp. 507–520, Sep. 2004. [Online]. Available: http://linkinghub.elsevier.com/retrieve/pii/S0034425704001828

[50] S. J. Katzberg, O. Torres, M. S. Grant, and D. Masters, "Utilizing calibrated GPS reflected signals to estimate soil reflectivity and dielectric constant: Results from SMEX02," *Remote Sens. Environ.*, vol. 100, no. 1, pp. 17–28, Jan. 2006. [Online]. Available: http://linkinghub.elsevier.com/retrieve/pii/S0034425705002932

[51] F. T. Ulaby, R. K. Moore, and A. K. Fung, *Microwave Remote Sensing: Active and Passive: Fundamentals and Radiometry*, vol. 1. 1981.

Alberto Alonso-Arroyo (S'11) was born in Barcelona, Spain. He received the M.S. degree in telecommunications engineering (B.Sc.+5) and the M.S. degree in research on information and communication technologies (M.Sc.+2) from the Universitat Politècnica de Catalunya, Barcelona, in 2011 and 2012, respectively, where he is currently pursuing the Ph.D. degree in GNSS-reflectometry with the Passive Remote Sensing Group, Department of Signal Theory and Communications.

He is currently with the National Oceanic and Atmospheric Administration, Boulder, CO, USA, as an Invited Visiting Researcher thanks to a Fulbright Grant.

Valery U. Zavorotny (M'01–SM'03–F'10) received the M.S. degree in radio physics from Gorky State University, Gorky, Russia, in 1971, and the Ph.D. degree in physics and mathematics from the Institute of Atmospheric Physics, USSR Academy of Sciences, Moscow, Russia, in 1979.

He is currently a Physicist with the Earth System Research Laboratory, National Oceanic and Atmospheric Administration, Boulder, CO, USA. He was with the Institute of Atmospheric Physics and the Lebedev Physical Institute, USSR Academy of Sciences, Moscow. He has over 150 publications in scientific journals, conference proceedings, and book chapters. His research interests include the areas of modeling of EM wave scattering from rough sea surface, ocean and land remote sensing applications using radar, and GNSS reflection techniques.

Dr. Zavorotny is currently a Co-Principal Investigator and a member of the Science Team for Cyclone Global Navigation Satellite System Mission, the project awarded by NASA in 2012 and planned for a launch in 2016. He is a member of AGU and a member of Commission F of the U.S. National Committee of URSI. He is a recipient of the Prince Sultan Bin Abdulaziz International Creativity Prize for Water, for the development of a new cost-effective technique, Global Positioning System Interferometric Reflectometry, to measure soil moisture, snow depth, and vegetation water content (together with K. Larson, E. Small, and J. Braun).

Adriano Camps (S'91–A'97–M'00–SM'03–F'11) was born in Barcelona, Spain, in 1969. He received the M.Sc. degree in telecommunications engineering and Ph.D. degree in telecommunications engineering from the Universitat Politècnica de Catalunya (UPC), Barcelona, in 1992 and 1996, respectively.

From 1991 to 1992, he was with the ENS des Télécommunications de Bretagne, Brest, France, with an Erasmus Fellowship. Since 1993, he has been with the Electromagnetics and Photonics Engineering Group, Department of Signal Theory and Communications, UPC, where he was first an Assistant Professor, then an Associate Professor in 1997, and where he has been a Full Professor since 2007. In 1999, he was on sabbatical leave at the Microwave Remote Sensing Laboratory, University of Massachusetts at Amherst, Amherst, MA, USA. Since 1993, he has been deeply involved in the European Space Agency SMOS Earth Explorer Mission, and since 2001 on the use of GNSS-R techniques to perform the sea state correction needed to retrieve salinity from radiometric observations. He has authored over 125 peer-reviewed journal papers and over 250 international conference presentations.

Dr. Camps has received a number of awards for his research and teaching activities, among which the Research Distinction of the Generalitat de Catalunya in 2002 for contributions to microwave passive remote sensing. He received the European Young Investigator Award of the European Science Foundation in 2004, the ICREA Academia Award in 2009, and the first and seventh Duran Farell Awards, in 2000 and 2010, respectively.